Available online at www.sciencedirect.com

jmr&t
Journal of Materials Research and Technology

journal homepage: www.elsevier.com/locate/jmrt

Original Article

Alloying effects on site preference, mechanical properties, and deformation behavior of $L1_2$ Co–Ti-based alloys

X.F. Gong [a], Z.H. Gao [a], L.P. Nie [a], S. Qiu [b,c,**], Q. Yu [b], H. Wu [d], G.P. Zheng [b], Z.B. Jiao [b,c,*]

[a] State Key Laboratory of Long-Life High Temperature Materials, Dongfang Electric Corporation Dongfang Turbine Co. Ltd., Deyang 618000, China
[b] Department of Mechanical Engineering, Research Institute for Advanced Manufacturing, The Hong Kong Polytechnic University, Hong Kong, China
[c] The Hong Kong Polytechnic University Shenzhen Research Institute, Shenzhen 518057, China
[d] State Key Laboratory of Powder Metallurgy, Central South University, Changsha 410083, China

ARTICLE INFO

Article history:
Received 9 January 2023
Accepted 13 March 2023
Available online 16 March 2023

Keywords:
Co-based alloy
Alloying effect
Phase stability
Mechanical property
First principles

ABSTRACT

Alloying plays an important role in controlling the phase stability, mechanical properties, and deformation behavior of ordered intermetallic compounds. In this study, the effects of 3*d*, 4*d*, and 5*d* transition elements on site preference, elastic properties, ideal shear strength, and planar fault energies of $L1_2$ Co–Ti-based alloys were systematically investigated by using first-principles calculations. The calculated transfer energy and formation enthalpy indicate that Sc, V, Cr, Y, Zr, Nb, Mo, W, Hf, Ta, and W tend to occupy the Ti site, which reduce the structural stability of $L1_2$-Co_3Ti. The elastic moduli and ideal shear strength of $L1_2$-Co_3(Ti,M) increase with average electron density. The electron localization function (ELF) analysis reveals that the Co–M bonds have a stronger covalent character than the Co–Ti bond, which plays an important role in the strengthening of the alloys. The ratio of superlattice intrinsic stacking fault (SISF) to anti-phase boundary (APB) energy of $L1_2$-Co_3(Ti,M) decreases with increasing atomic number of alloying elements in each period in the range of studied elements, which tends to change the deformation mode from the APB-favored to SISF-favored ones. The APB anisotropy ratio of $L1_2$-Co_3(Ti,M) decreases with increasing atomic number of alloying elements in each period, which enhances the yield strength anomaly. This study not only sheds insight into the fundamental understanding of phase stability and mechanical behavior of multicomponent $L1_2$ compounds, but also provides useful guidelines for designing novel $L1_2$-stregnthened Co-based superalloys with superior mechanical properties.

* Corresponding author.
** Corresponding author.
E-mail addresses: shiqiu.qiu@polyu.edu.hk (S. Qiu), zb.jiao@polyu.edu.hk (Z.B. Jiao).
https://doi.org/10.1016/j.jmrt.2023.03.099

1. Introduction

High-temperature superalloys are critical materials for numerous demanding applications in the energy and aerospace sectors. With the increasing performance needs for advanced jet engine and gas turbine applications, the development of advanced superalloys with higher temperature capacity is essential. The inherent operation temperature of Ni-based superalloys is limited by the melting point of Ni, its primary element, which has a melting temperature of ~1455 °C [1,2]. Co-based superalloys have emerged as a promising candidate for next-generation high-temperature turbine blade materials because the melting point of Co (~1495 °C) is higher than that of Ni [3]. In 2006, Sato et al. [4] developed a γ(fcc)/γ'($L1_2$) microstructure in the Co–Al–W system, in which coherent $L1_2$-Co_3(Al,W) precipitates form in the fcc matrix, similar to the microstructure of Ni-based superalloys. The $L1_2$-strengthened Co–Al–W-based superalloys possess higher creep strength than conventional solute-strengthened Co-based superalloys [5]. In addition, this new class of $L1_2$-strengthened materials have higher solidus and liquidus temperatures and exhibit less segregation during solidification compared to traditional Ni-based superalloys [6], which thus opens a new avenue for developing novel superalloys with superior high-temperature properties [4]. However, Co–Al–W-based superalloys suffer from several problems, such as insufficient stability [7], narrow compositional range [4], and high density [8], which limits the practical applications of these materials. Therefore, the exploration of novel Co-based superalloys with low density and stable $L1_2$ precipitates is urgent and highly in demand.

The Co–Ti-based alloy system has shown to be an alternative to the Co–Al–W system because the $L1_2$-Co_3Ti phase is thermodynamically stable in the available binary Co-based alloys [9]. Additionally, Co_3Ti exhibits a positive temperature-dependence yield strength (namely yield strength anomaly) between 200 and 800 °C, which is expected for an excellent reinforcement phase for high-temperature structural materials [10]. However, there are several critical issues that need to be addressed for the $L1_2$-Co_3Ti-strengthened superalloys to become practical engineering materials. These issues include the exceedingly large fcc/$L1_2$ lattice misfit (1.2%) [11], low $L1_2$ volume fractions (20% at 900 °C), and low solvus temperatures (~1005 °C) [12], which hinder the use of $L1_2$-Co_3Ti in Co-based superalloys. To solve these critical issues, considerable efforts have been made to develop new Co–Ti-based superalloys through alloying. For example, Co–Ti–Cr superalloys exhibit a higher solvus temperature and a larger volume fraction of $L1_2$ phases than those of binary Co–Ti alloys [13]. Particularly, alloying Cr significantly declines the fcc/$L1_2$ lattice misfit of the alloys, thereby changing the $L1_2$ morphology from irregular shape to nearly cubic shape [12]. Mo was found to strongly partition to the Ti sublattice of the $L1_2$ phase, which makes the alloys exhibit a strong yield strength anomaly and work hardening capacity [11]. In addition, V was reported to not only stabilize the $L1_2$ phase at high temperatures, but also improves the strength of Co–Ti-based alloys [3]. Although alloying has been shown to be an efficient way to control the precipitate microstructure and mechanical properties of $L1_2$-strengthened Co-based superalloys, an in-depth understanding of alloying effects on the site occupation, mechanical properties, and deformation behavior of $L1_2$-Co_3Ti remains incomplete.

In this work, the effects of transition metal elements, including Sc, V, Cr, Y, Zr, Nb, Mo, W, Hf, Ta, and W, on the site preference, lattice constants, structural stability, elastic properties, ideal shear strength, and planar fault energies of $L1_2$-Co_3Ti were thoroughly studied using first-principles calculations based on the density functional theory. Specifically, the alloying effects on the elastic properties, ideal shear strength, and chemical bonding characters were evaluated to probe the strengthening mechanisms. The planar fault energies, including the superlattice intrinsic stacking fault (SISF) energy and anti-phase boundary (APB) energy, were calculated to determine the preferred deformation mode and possibility for the occurrence of yield strength anomaly. The emphasis was placed on the fundamental understanding of the alloying effects on the site preference, structural stability, mechanical properties, and deformation behavior of $L1_2$-Co_3Ti.

2. Theoretical methods

2.1. Computational details of first-principles calculations

All the first-principles calculations were performed by using Vienna *Ab initio* Simulation Package (VASP) [14] with Perdew-Burke-Enzerhoff (PBE) exchange-correlation functional in generalized gradient approximation (GGA) [15]. Convergence tests were performed to ensure total energy convergence as a function of cutoff energy (see Supplementary Table S1). From the convergence tests, the cut-off energy of 450 eV ensures that the computational error of total energy is lower than 1 meV/atom and thus was used in this study. The Brillouin-zone sampling were performed by Gamma-centered k-meshes with grid spacing of below 0.03 $Å^{-1}$. The convergence accuracy of energy was below 10^{-5} eV/atom, and the maximum force of ionic relaxation was set to below 0.02 eV/Å. Spin polarization was considered throughout the first-principles calculations.

2.2. Site preference and structural stability

The concept of transfer energy proposed by Ruban et al. [16] has been extensively used to evaluate the site substitution preference of alloying elements in $L1_2$-type phases [17–21]. The transfer energy of a 32-atom supercell can be given by

$$E^{M}_{Co\rightarrow Ti} = E(Co_{24}Ti_7M) + E(Co_{23}Ti_9) - E(Co_{23}MTi_8) - E(Co_{24}Ti_8) \quad (1)$$

where $E^{M}_{Co\rightarrow Ti}$ represents the energy of moving one M atom from the Co to Ti site, E ($Co_{24}Ti_8$) is energy of the stoichiometric $Co_{24}Ti_8$ structure, E ($Co_{23}Ti_9$) is the energy of $Co_{23}Ti_9$ with one Ti antisite, and E ($Co_{23}MTi_8$) and E ($Co_{24}Ti_7M$) are the energies of $L1_2$-Co_3Ti with an M atom in the Co and Ti sites, respectively. The normalized transfer energy (E_{trans}) is given by

$$E_{trans} = E^{M}_{Co\rightarrow Ti} / E_{defect} \quad (2)$$

where E_{defect} is the energy of exchange defect formation, which is expressed as

$$E_{defect} = E(Co_{23}Ti_9) + E(Co_{25}Ti_7) - 2E(Co_{24}Ti_8) \quad (3)$$

where E ($Co_{25}Ti_7$) is the energy of $L1_2$-Co_3Ti with one Co antisite. According to Ruban et al. [10], the site preference of alloying elements can be determined as follows: (1) $E_{trans} < 0$ for a strong Ti site preference, (2) $0 < E_{trans} < 0.5$ for a weak Ti site preference, (3) $0.5 < E_{trans} < 1$ for a weak Co site preference, and (4) $E_{trans} > 1$ for a strong Co site preference.

The formation enthalpy (ΔH) was used to evaluate the phase stability of the $L1_2$-Co_3Ti structures [22]. Taking M occupying the Ti site as an example, the formula is expressed as:

$$\Delta H = E(Co_{24}Ti_7M) - 7E(Ti) - 24E(Co) - E(M) \quad (4)$$

where E ($Co_{24}Ti_7M$) is the total energy of $L1_2$-$Co_{24}Ti_7M$, and E (Ti), E (Co), and E(M) are the total energies of hcp-Ti, hcp-Co, and M in their stable state, respectively. Here, M = V, Cr, Nb, Mo, Ta and W have a bcc structure, while M = Sc, Y, Zr, and Hf have an hcp structure. In addition, previous studies reported that the $D0_{19}$-type phase is a common competitor against the $L1_2$-type phase in Co-based superalloys [4,18]. Thus, the formation energies of 64-atom supercells with a $D0_{19}$ structure were also evaluated and compared with those of the 32-atom supercells with a $L1_2$ structure.

2.3. Elastic properties

The strain–stress method was used to calculate a series of elastic constants. A set of strains were imposed on a 32-atom supercell to generate slight deformations, and corresponding stresses were obtained. The stresses and strains satisfy Hooke's law under small deformations [23]. For more details of the strain–stress method, readers are referred to Ref. [24]. Two deformation intervals, i.e., ±0.01 and ± 0.015, were tested, and the results from the two intervals are quite comparable (see Supplementary Table S2). Thus, the interval of ±0.01 was finally used in the analysis. For the cubic symmetry, the three independent elastic constants (C_{11}, C_{12} and C_{44}) were obtained, and the Young's modulus, shear modulus, and bulk modulus were calculated based on Voigt's and Reuss's approximations to limit the upper and lower bounds. The approximations assume that the strain and stress in the polycrystals are uniform [25]. According to Hill's approach with the average of the Voigt's and Reuss's approximations, the shear modulus (G) and bulk modulus (B) can be obtained by Ref. [26].

$$G = (G_v + G_R)/2, G_v = (C_{11} - C_{12} + 3C_{44})/5 \text{ and } G_R = 5/(4S_{11} - 4S_{12} + 3S_{44}) \quad (5)$$

$$B = (B_v + B_R)/2, B_v = (C_{11} + 2C_{12})/3 \text{ and } B_R = 1/(3S_{11} + 6S_{12}) \quad (6)$$

where S_{ij} is the elastic compliance constant and can be obtained by inverting the matrix of [C_{ij}]. Furthermore, the Young's modulus (E) is given by

$$E = 9BG/(3B + G) \quad (7)$$

2.4. Ideal shear strength

Previous theoretical studies and experimental observations showed that (1 1 1) is the most preferable slip plane for $L1_2$-type phases, such as Co_3Ti, Ni_3Al, and $Co_3(Al,W)$ [10,27]. Thus, the shear deformation of the 32-atom supercell on the (1 1 1) plane along the [1 1 −2] direction was used to investigate the alloying effects on the micro-scale shear deformation of $L1_2$-Co_3Ti in the present study. We used the lattice rotation method to calculate the ideal shear strength; this method has been widely used in the literature [27,28]. Specifically, we built a 32-atom $Co_{24}Ti_7M$ supercell, as illustrated in Fig. 1a. The schematic diagram of lattice rotation for the (1 1 1) plane is shown in Fig. 1b. The lattice was rotated around z, y, and x axes with $\alpha = -45°$, $\beta = 35.26°$, and $\gamma = 180°$, respectively, to set (1 1 1)[1 1 −2] as the shear direction. The shear stress (τ) can be calculated by a series of incremental shear strains, as proposed by Roundy et al. [29], which can be obtained by

$$\tau = \frac{1}{V}\frac{\partial E}{\partial \varepsilon} \quad (8)$$

where ε is the shear strain, and V and E are the volume and energy of the system, respectively. At each strain step, the configurations were relaxed in all directions except in the

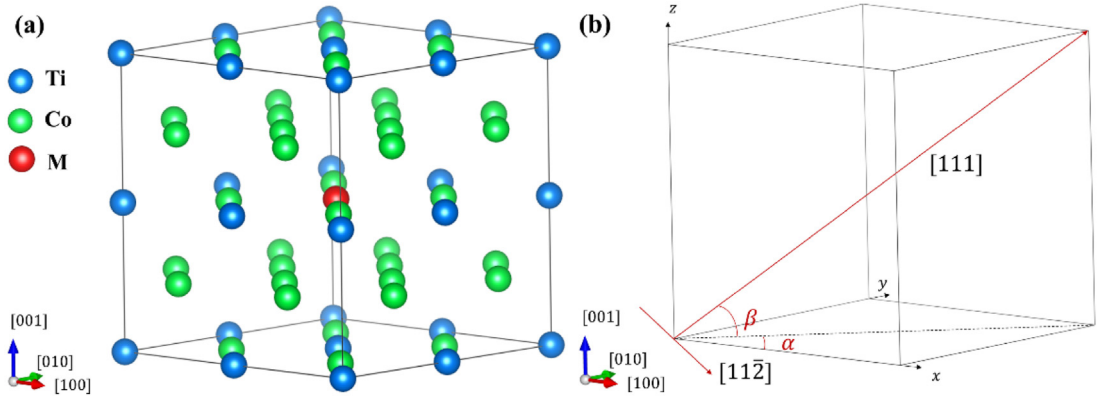

Fig. 1 – Schematic diagrams of (a) $L1_2$-type supercells used for the calculation of ideal shear stress and (b) lattice rotation for the (1 1 1) plane.

direction of the applied strain. The ideal shear stress can be determined when τ reaches to the first maximum value.

2.5. *Planar fault energy*

The construction of planar fault structures, including the (1 1 1) APB, (1 1 1) SISF, and (0 1 0) APB, was based on the alias shear deformation method, in which only one atomic plane moves along the Burgers vector [30]. The (1 1 1) APB can be generated by the tilting lattice vector [1 1 1] of an ideal $L1_2$ structure along the [−1 0 1] direction by $a_0/2$ [−1 0 1], as illustrated in Fig. 2a. Tilting the lattice vector [1 1 1] along the [−1 −1 2] direction by $a_0/3$ [−1 −1 2] results in the (1 1 1) SISF (see Fig. 2b). The (0 1 0) APB can be generated by an alias shear deformation on the (0 1 0) plane along the [−1 0 1] direction by $a_0/2$ [−1 0 1] (see Fig. 2c). The planar fault energy (γ_{PF}) of the $L1_2$-type supercells was evaluated by calculating the energy difference between the perfect and planar faulted models, which can be expressed by

$$\gamma_{PF} = (E_{PF} - E_{L12}) / A_{area} \quad (9)$$

where E_{PF} is the energy of fault structures, while E_{L12} is the energy of the ideal $L1_2$ structures, A_{area} is the area of the supercell fault plane. For the perfect structure, all the atomic positions and supercell geometries were fully relaxed. For the planar faulted structures, the supercell geometries were kept fixed, whereas the atomic positions were relaxed. The effect of supercell size on the planar fault energy of Co_3Ti was tested to ensure that planar faults do not interact with each other due to the periodic boundary conditions (see Supplementary Table S3), and after the test we chose the planar fault structures of (1 1 1) APB, (1 1 1) SISF, and (0 1 0) APB with 9, 9, and 10 atomic layers, respectively. To study the influence of solute position on the fault energies, we calculated the APB energy of the $Co_{24}Ti_7M$ supercells with solute atoms in different atomic layers with respect to the fault plane (see Supplementary Fig. S1). It is seen that the solute effect on the APB energy is localized in the first nearest atomic layers to the fault plane, and thus we used a solute atom to replace a Ti atom in the two nearest atomic layers along the planar fault. Since each atomic layer has 8 atoms, the alloying concentration in the two nearest atomic layers with respect to the planar fault is 6.25 at.%.

3. Results and discussion

3.1. *Site preference, lattice constant, and structural stability*

The normalized transfer energies (E_{trans}) of 3*d*, 4*d* and 5*d* transition elements in $L1_2$-Co_3Ti were calculated based on Eqs. (1)–(3), and the results are shown in Fig. 3 and Table 1. All the E_{trans} are below 0.5, indicating that all the studied transition elements prefer to occupy the Ti site. Except for Sc and Y that exhibit a weak Ti-site occupancy, all other transition elements (V, Cr, Zr, Nb, Mo, Hf, Ta, and W) show a strong Ti-site preference. Im et al. [12] studied the γ' site-occupancy behavior of solute elements in the Co–Ti system by means of atom probe tomography (APT), and their results reveal that both Mo and Cr preferentially replace Ti in the $L1_2$-Co_3Ti structure. Our calculation results are in good agreement with the APT observation.

In binary Co–Ti alloys, the large lattice of $L1_2$-Co_3Ti causes an exceedingly high lattice misfit between $L1_2$-Co_3Ti and fcc-Co, leading to the fast coarsening of $L1_2$ precipitates and degeneration of high-temperature strength [31]. Thus, decreasing the lattice constant of $L1_2$ phases is necessary for the design of novel Co–Ti-based superalloys. The alloying effects on lattice constant of $L1_2$-Co_3(Ti,M) were calculated, and the results are displayed in Fig. 4 and Table 1. Our calculated lattice constant of stoichiometric $L1_2$-Co_3Ti is 3.606 Å, which agrees with previous theoretical results (3.61 Å) and experimental values (3.597 Å), with a deviation of less than 0.3% [32,33]. The result demonstrates a good reliability and accuracy of the present calculations. From Fig. 4 it is seen that the lattice constant of $L1_2$-Co_3(Ti,M) decreases with increasing atomic number in each period in the range of studied elements. To further illustrate how the alloying elements influence the lattice constant of $L1_2$-Co_3(Ti,M), we explored the relationship between the atomic radius of solute

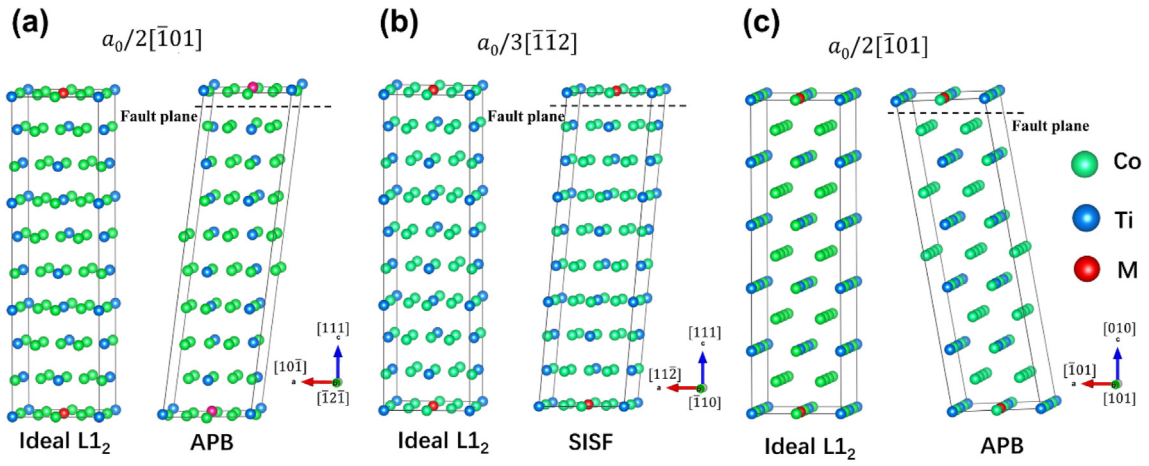

Fig. 2 – Schematic diagrams of $L1_2$-type supercells used for the calculation of planar fault energies, with (a) for an APB on the (1 1 1) plane, (b) for an SISF on the (1 1 1) plane, and (c) for an APB on the (0 1 0) plane.

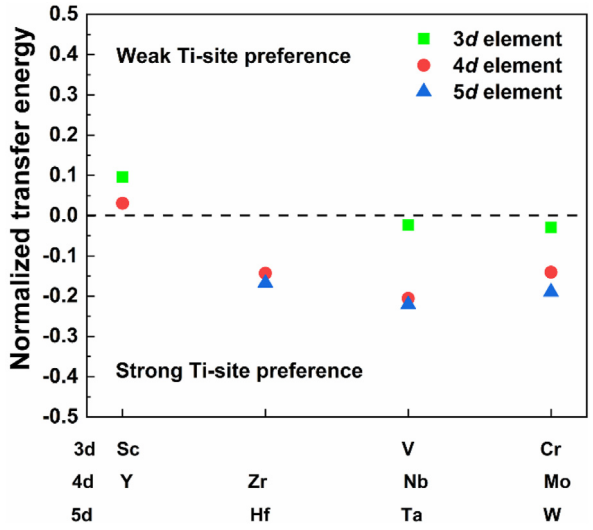

Fig. 3 – Normalized transfer energies of transition elements (Cr, Mo, W, V, Nb, Ta, Zr, Hf, Sc, and Y) in $L1_2$-Co_3Ti.

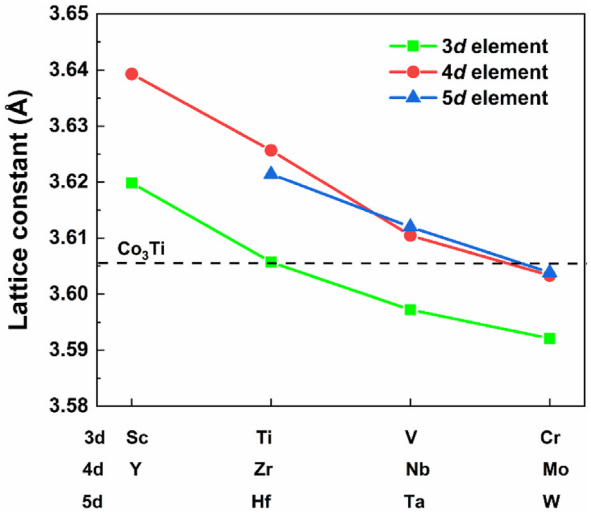

Fig. 4 – Lattice constants of $L1_2$-$Co_{24}(Ti_7M)$ (M = Cr, Mo, W, V, Nb, Ta, Zr, Hf, Sc, and Y).

M and lattice constant of $L1_2$-$Co_{24}(Ti_7M)$, and the result is shown in Supplementary Fig. S2. The result indicates that the lattice constant of $L1_2$-$Co_{24}(Ti_7M)$ increases with increasing atomic radius of alloying elements in each period in the range of studied elements. Considering that $L1_2$-Co_3Ti has a larger lattice constant than fcc-Co [34], the partitioning of V, Cr, Mo, and W to the $L1_2$ phase decrease its lattice constant, which would be beneficial in reducing the lattice misfit between the $L1_2$-Co_3Ti and fcc-Co phases. Our calculation results are in good agreement with the experimental observations, which revealed that Mo, V and W decrease the Co/Co_3Ti lattice misfit [12,34,35]. It should be pointed out that the partitioning of alloying elements to the fcc matrix can also affect the lattice misfit between the $L1_2$ and fcc phases. For example, Li et al. [36] reported that Re prefers to partition to the γ matrix in the Co–Ti–Re alloys, which increases the lattice constant of the γ matrix, thereby decreasing the lattice misfit between the γ′ precipitates and γ matrix.

Table 1 – Calculated lattice constants (a_0), normalized transfer energies (E_{trans}), formation enthalpies (ΔH), and energy differences ($E_{D019\rightarrow L12}$) between the $L1_2$ and $D0_{19}$ structures for $Co_{24}(Ti_7M)$ (M = Cr, Mo, W, V, Nb, Ta, Zr, Hf, Sc, and Y).

Compound	a_0 (Å)	E_{trans}	ΔH (eV/atom)	$E_{D019\rightarrow L12}$ (eV/atom)
$Co_{24}Ti_8$	3.606	–	−0.259	−0.034
Calc [32]	3.61	–	−0.262	−0.037
Expt [33]	3.597	–	–	–
$Co_{24}(Ti_7Sc)$	3.620	0.095	−0.234	−0.030
$Co_{24}(Ti_7Y)$	3.639	0.031	−0.196	−0.026
$Co_{24}(Ti_7Zr)$	3.626	−0.143	−0.240	−0.030
$Co_{24}(Ti_7Hf)$	3.621	−0.167	−0.252	−0.031
$Co_{24}(Ti_7V)$	3.597	−0.024	−0.248	−0.031
$Co_{24}(Ti_7Nb)$	3.610	−0.206	−0.246	−0.029
$Co_{24}(Ti_7Ta)$	3.612	−0.221	−0.254	−0.031
$Co_{24}(Ti_7Cr)$	3.592	−0.029	−0.227	−0.024
$Co_{24}(Ti_7Mo)$	3.603	−0.141	−0.231	−0.025
$Co_{24}(Ti_7W)$	3.604	−0.189	−0.237	−0.028

To evaluate the alloying effects on structural stability of $L1_2$-$Co_3(Ti,M)$, the formation enthalpy (ΔH) was calculated using Eq. (4), and the results are listed in Table 1. A negative ΔH of $L1_2$-Co_3Ti indicates the $L1_2$-Co_3Ti phase is more stable than its constitutional elements. It should be noted that the alloying concentration (3.1 at.%) is not high, and higher concentrations of alloying elements may destabilize the $L1_2$ structure. Thus, the control of alloying concentrations is also important for controlling thermodynamic stability of $L1_2$ phases in Co–Ti-based superalloys.

Considering that the $D0_{19}$ phase is a potential competitor against the $L1_2$ phase in Co-based superalloys, the energy difference between the $L1_2$ and $D0_{19}$ structures ($E_{D019\rightarrow L12}$) was calculated, and the results are summarized in Table 1. The energy difference between the $L1_2$ and $D0_{19}$ Co_3Ti is −0.034 eV/atom, which agrees well with previously reported theoretical data (−0.037 eV/atom) [32]. With alloying additions, the energy difference between the $L1_2$ and $D0_{19}$ structures increases. Particularly, the energy difference increases from −0.034 eV/atom for $Co_{24}Ti_8$ to −0.024 eV/atom for $Co_{24}(Ti_7Cr)$ and to −0.025 eV/atom for $Co_{24}(Ti_7Mo)$. In other words, the alloying elements have a negative effect on the structural stability of $L1_2$-Co_3Ti, which is also consistent with the experimental observation that Co–Ti is the only reported binary alloy system with a thermodynamically stable $L1_2$ structure [9,35].

3.2. *Alloying effects on mechanical properties*

3.2.1. *Elastic moduli*

Elastic moduli, including Young's modulus (E), shear modulus (G), and bulk modulus (B), are known as important parameters that determine materials properties, such as toughness [37] and strength [38]. Before discussing elastic moduli, it is necessary to understand the alloying effects on elastic constants (C_{ij}) of $L1_2$-Co_3Ti. For a cubic symmetry, the three independent elastic constants (i.e., C_{11}, C_{12}, and C_{44}) were

Table 2 – Elastic constants (C_{11}, C_{12} and C_{44}), Young's modulus (E), shear modulus (G), bulk modulus (B), bonding valences (Z_B), volumes (V), and average electron densities (n) of $L1_2$-$Co_{24}Ti_8$ and $Co_{24}(Ti_7M)$.

Compound	C_{11} (GPa)	C_{12} (GPa)	C_{44} (GPa)	E (GPa)	G (GPa)	B (GPa)	Z_B (el)	V (Å^3)	n (el/Å^3)
$Co_{24}Ti_8$	263	161	121	224	86	195	3.118	11.719	0.266
Calc [32]	258	162	119	217	83	194	–	–	–
Calc [39]	260	168	119	222	84	201	–	–	–
$Co_{24}(Ti_7Sc)$	254	155	113	213	81	188	3.107	11.858	0.262
$Co_{24}(Ti_7Y)$	249	155	105	201	76	186	3.118	12.050	0.259
$Co_{24}(Ti_7Zr)$	263	160	116	219	84	194	3.135	11.916	0.263
$Co_{24}(Ti_7Hf)$	266	161	117	223	85	196	3.142	11.873	0.265
$Co_{24}(Ti_7V)$	271	159	124	235	90	197	3.125	11.637	0.269
$Co_{24}(Ti_7Nb)$	278	168	123	233	89	205	3.147	11.766	0.267
$Co_{24}(Ti_7Ta)$	275	165	123	233	89	202	3.158	11.781	0.268
$Co_{24}(Ti_7Cr)$	273	160	127	238	92	198	3.128	11.587	0.270
$Co_{24}(Ti_7Mo)$	273	164	127	236	91	200	3.156	11.696	0.270
$Co_{24}(Ti_7W)$	274	164	128	237	91	201	3.167	11.701	0.271

calculated, which are listed in Table 2. Our calculated C_{11}, C_{12}, and C_{44} of stoichiometric $L1_2$-Co_3Ti are in good agreement with previously reported theoretical data with a deviation of no more than 2% [32,39]. With the alloying additions, the elastic constants change. Even so, all the calculated elastic constants of $L1_2$-$Co_{24}(Ti_7M)$ satisfy the Born stability criteria, i.e., $C_{11} > 0$, $C_{44} > 0$, $C_{11} > |C_{12}|$, and $C_{11} + 2C_{12} > 0$, indicating that they are all mechanically stable.

The effect of alloying elements on the Young's modulus (E), shear modulus (G), and bulk modulus (B) of $L1_2$-Co_3(Ti,M) were evaluated, and the results are summarized in Table 1 and Fig. 5. It is apparent that the Young's modulus (Fig. 5a) and shear modulus (Fig. 5b) increase progressively with increasing atomic number of alloying elements. The bulk modulus shows a similar variation trend except for Nb and Ta (Fig. 5c). Based on the calculated elastic properties, the intrinsic ductility/brittleness of $L1_2$-Co_3(Ti,M) can be evaluated using an empirical Pugh ratio (B/G). Generally, alloys are ductile if the Pugh ratio is higher than 1.75, while materials tend to be brittle if the Pugh ratio is below this critical value. Cauchy pressure ($C_{11}-C_{12}$) is an empirical parameter in predicting the bonding characteristics [40]. A positive Cauchy pressure value indicates an intrinsically ductile behavior of alloys with non-directional metallic bonds, while a negative value suggests an intrinsically brittle behavior of alloys with directional covalent bonds. Fig. 5d illustrates the relationship between the Pugh ratio and Cauchy pressure for $L1_2$-$Co_{24}(Ti_7M)$. Apparently, the Pugh ratio is linearly proportional to the Cauchy pressure. All the Pugh ratios are higher than 2.16, and all the Cauchy pressures are larger than 33 GPa, indicating an intrinsically ductile nature of the $Co_{24}(Ti_7M)$ alloys. It is worth noting that the alloys tend to become more ductile with decreasing atomic number in each period in the range of studied elements. In particular, Cr, Mo, W, and V increase the elastic moduli of the $Co_{24}(Ti_7M)$ alloys but deteriorate their ductile performance.

Previous works showed that there is an empirical relationship between the bulk modulus (B) per equilibrium volume (V) and average electron density (n); that is, $(B/V)^{0.5}$ is linearly proportional to n for $L1_2$-Ni_3Al and Co_3(Al,W) [26,41]. This finding indicates that the average electron density of $L1_2$ phases may be one important factor determining the elastic properties. Considering that the elastic properties of $L1_2$-$Co_{24}(Ti_7M)$ are closely related to the atomic number of alloying elements as discussed above, it is interesting to understand the alloying effects on the average electron density and elastic properties of $L1_2$-$Co_{24}(Ti_7M)$. The values of average electron density for pure elements can be obtained via $n = Z_B/V$, where Z_B is the bonding valence, and V is the equilibrium volume. By using the rule-of-mixture approach, the average electron density of $L1_2$-$Co_{24}(Ti_7M)$ (M = Cr, Mo, W, V, Nb, Ta, Zr, Hf, Sc, and Y) can be obtained by

$$n(Co_{24}Ti_7M) = Z_B(Co_{24}Ti_7M) \,/\, V(Co_{24}Ti_7M) \tag{10}$$

$$Z_B(Co_{24}Ti_7M) = \frac{24}{32}Z_B(Co) + \frac{7}{32}Z_B(Ti) + \frac{1}{32}Z_B(M) \tag{11}$$

With input values of bonding valence of constitute elements (Z_B(Co), Z_B(Ti), and Z_B(M)) [42], the calculated $Z_B(Co_{24}Ti_7M)$ and $V(Co_{24}Ti_7M)$ are listed in Table 2. The relationship between the average electron density and elastic modulus of $L1_2$-$Co_{24}Ti_7M$ is plotted in Fig. 6. It is seen that the values of Young's modulus (Fig. 6a) and shear modulus (Fig. 6b) increase almost linearly with the average electron density of $L1_2$-$Co_{24}Ti_7M$. $(B/V)^{0.5}$ is roughly linearly proportional to n for $L1_2$-$Co_{24}Ti_7M$ (Fig. 6c), which is in agreement with previous works [26,41]. In contrast, the Pugh ratio decreases with increasing average electron density (Fig. 6d). Therefore, a high atomic number of alloying elements in each period in the range of studied elements contributes to a large average electron density of $L1_2$-$Co_{24}Ti_7M$, which tends to increase the Young's modulus, shear modulus, and bulk modulus but decreases the Pugh ratio of $L1_2$-$Co_{24}Ti_7M$.

3.2.2. *Ideal shear strength*

The ideal shear strength (τ) can be calculated by the first maximum point of the strain–stress curve during shear deformation, which is related to the multiplication of dislocations and the minimum stress attained to cause permanent deformation in a material without imperfections [43,44]. In the $L1_2$-strengthened superalloys, the ideal shear strength of $L1_2$ phases is essential to understand the strengthening mechanism of superalloys [43]. The ideal shear strengths of $L1_2$-$Co_{24}Ti_7M$ were calculated along the [1 1–2] shear direction on

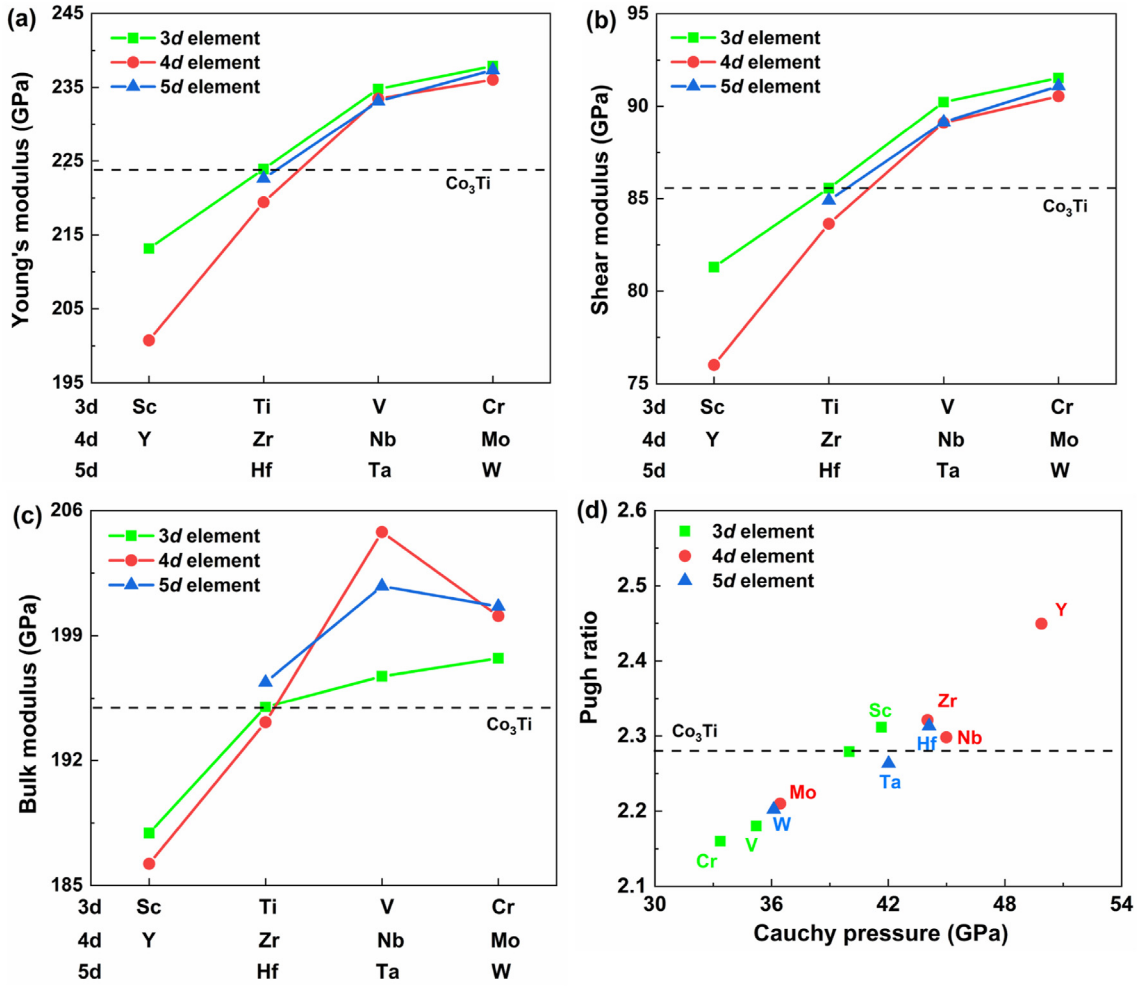

Fig. 5 – (a) Young's modulus (*E*), (b) shear modulus (*G*), (c) bulk modulus (*B*), and (d) relationship between Pugh ratio (*B*/*G*) and Cauchy pressure (C_{11}–C_{12}) of $L1_2$-$Co_{24}(Ti_7M)$ (M = Cr, Mo, W, V, Nb, Ta, Zr, Hf, Sc, and Y).

the (1 1 1) plane, and the results are displayed in Fig. 7. Before demonstrating the alloying effects, we first plotted the strain–stress curves of the stoichiometric $L1_2$-Ni_3Al and Co_3Ti as well as the available theoretical results for comparison (Fig. 7a). Our calculated ideal shear strength of $L1_2$-Ni_3Al is 3.8 GPa, which is in good agreement with previous studies by Chen et al. (4.2 GPa), Shang et al. (3.7 GPa), and Xia et al. (3.8 GPa) [27,43,45]. Our predicted ideal shear strength of the stoichiometric $L1_2$-Co_3Ti is 6.5 GPa, which is much larger than that of $L1_2$-Ni_3Al (3.8 GPa), demonstrating that the Co–Ti bond has strong resistance to plastic deformation and breaking. With alloying additions, the ideal shear strengths are in the range of 5.5–7.6 GPa. The variation trend of ideal shear strength (Fig. 7b) is similar to that of shear modulus (cf. Fig. 5b), suggesting that alloying V, Nb, Ta, Cr, Mo, and W to $L1_2$-Co_3Ti can significantly improve the ideal shear strength.

The relationship between the normalized ideal shear strength and Pugh ratio of $L1_2$-$Co_{24}(Ti_7M)$ is shown in Fig. 8. The $L1_2$-$Co_{24}(Ti_7M)$ compounds with strong resistance to shear deformation also exhibit a reduced ductility, as evidenced by the low Pugh ratios. In particular, the $L1_2$-$Co_{24}(Ti_7M)$ with additions of Cr, W, V, Mo and Ta have a higher ideal shear strength but a lower Pugh ratio than the stoichiometric $L1_2$-Co_3Ti, whereas alloying with Hf, Zr, Sc, and Y leads to a lower ideal shear strength but a higher Pugh ratio. The $L1_2$-$Co_{24}(Ti_7Nb)$ appears to have both a slightly higher shear strength and higher ductility than the stoichiometric $L1_2$-Co_3Ti. There is a general trend that the ideal shear strength increases with increasing average electron density of $Co_{24}(Ti_7M)$, which is similar to the aforementioned variation trend of elastic moduli.

3.2.3. *Electronic structure*

To understand the mechanism for the increased elastic moduli and ideal shear strength of $Co_{24}(Ti_7M)$ with increasing average electron density (*n*), the characteristics of chemical bonding in the $L1_2$-$Co_{24}(Ti_7M)$ structures were investigated by using the electron localization function (ELF). The ELF is an important tool to study the electronic structure, which can provide quantitative information on the chemical bonding of compounds [46–48]. Generally, the ELF = 1 means that electrons are perfectly localized between two adjacent atoms, while ELF = 0.5 represents an electron-gas-like pair probability. In the metallic system, ELF is mainly in the range between

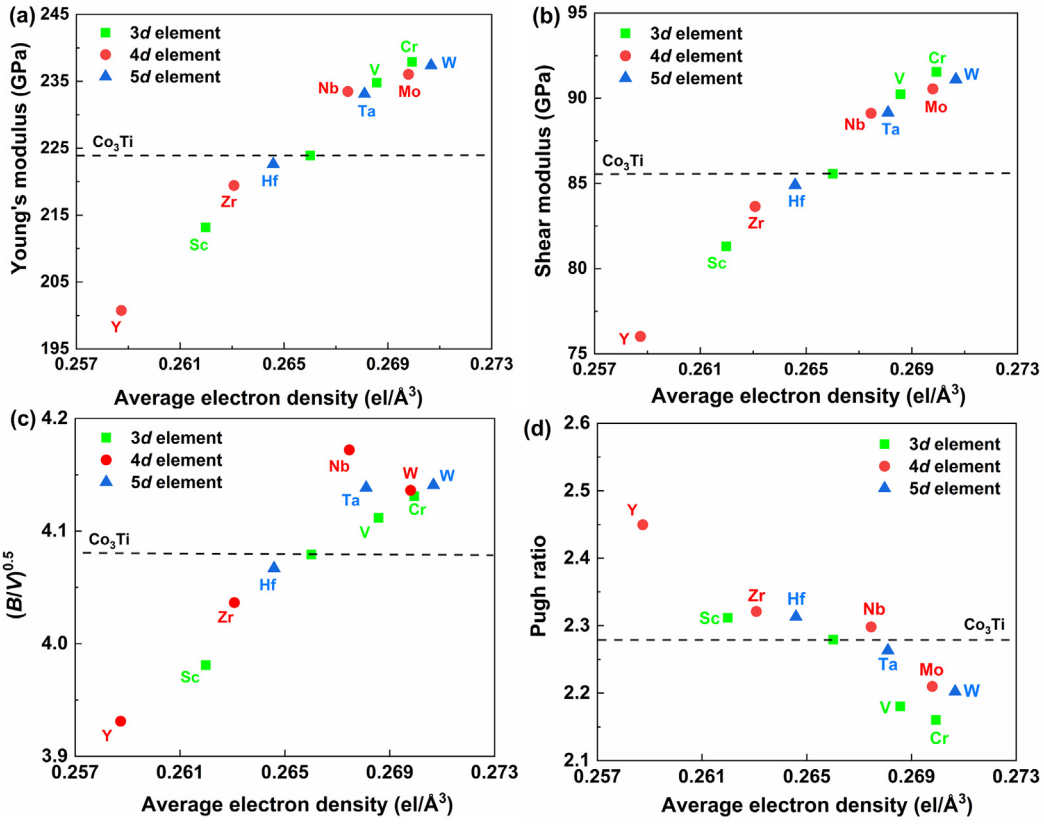

Fig. 6 – (a) Young's modulus (*E*), (b) shear modulus (*G*), (c) $(B/V)^{0.5}$, where *B* and *V* are bulk modulus and volume, respectively, and (d) Pugh ratio (*B*/*G*) as a function of average electron density of $L1_2$-$Co_{24}(Ti_7M)$ (M = Cr, Mo, W, V, Nb, Ta, Zr, Hf, Sc, and Y).

0 and 0.5, and a high ELF between two adjacent atoms indicates a strong chemical bonding. Taking Cr and Mo as the representative alloying elements, the contour of ELF projected on the (1 1 1) plane of $Co_{24}Ti_8$, $Co_{24}(Ti_7Cr)$, and $Co_{24}(Ti_7Mo)$ with an average electron density of 0.266, 0.270, and 0.270 el/Å^3 is shown in Fig. 9. We marked the ELF values around Co by a dashed rectangle. Clearly, the ELF values around Co increase when Ti is replaced by Cr and Mo. This finding indicates that

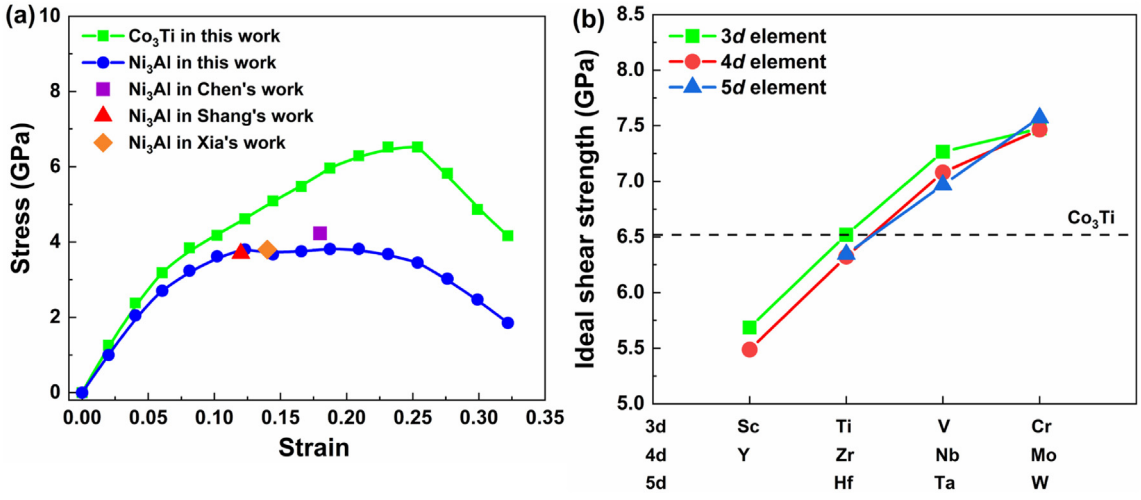

Fig. 7 – (a) Strain–stress curves of $L1_2$-Ni_3Al and Co_3Ti along the [1 1 −2] shear direction on the (1 1 1) plane, and (b) ideal shear strength (τ) of $L1_2$-$Co_{24}(Ti_7M)$ (M = Cr, Mo, W, V, Nb, Ta, Zr, Hf, Sc, and Y). The available data of ideal shear strength of $L1_2$-Ni_3Al by Chen et al. [27], Shang et al. [43], and Xia et al. [45] is included in Fig. 7a.

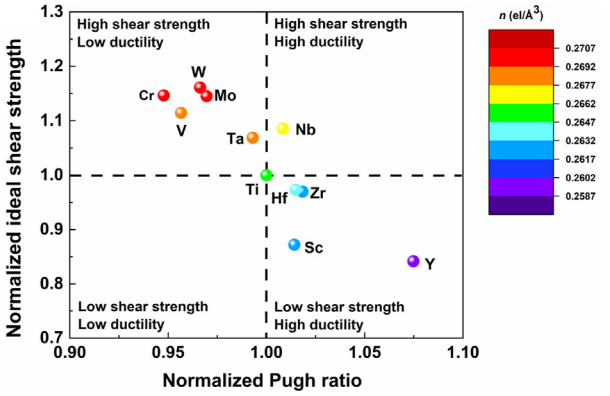

Fig. 8 – Normalized ideal shear strength and Pugh ratio of $L1_2$ $Co_{24}(Ti_7M)$ (M = Cr, Mo, W, V, Nb, Ta, Zr, Hf, Sc, and Y) and Co_3Ti. *n* represents average electron density of $Co_{24}(Ti_7M)$.

the electron localizations between Co and Cr/Mo are enhanced, indicating that the Co–Cr and Co–Mo bonds have a stronger covalent character than the Co–Ti bond. Meanwhile, alloying with Cr and Mo does not result in a significant change in the Co–Ti bond. Therefore, the strengthening effect of the alloying additions is due mainly to the strong covalent-like bonding between Co and alloying elements.

3.3. *Deformation behavior*

3.3.1. *Deformation mode*

The deformation behavior of $L1_2$ phases in superalloys are strongly influenced by their planar faults (such as anti-phase boundaries (APBs) and superlattice intrinsic stacking faults (SISFs)) created during the shearing of the $L1_2$ phases under service conditions, which significantly affects the high-temperature strength of $L1_2$-strengthened superalloys [49]. In the $L1_2$-type structure, the parent [−1 0 1] dislocation on the (1 1 1) plane can dissociate in the APB and SISF modes [49,50]. In the APB mode, the [−1 0 1] dislocation splits into a pair of 1/2 [-1 0 1] superpartial dislocations separated by an APB, which can be described by

$$[\bar{1}01] \rightarrow \frac{1}{2}[\bar{1}01] + \mathrm{APB} + \frac{1}{2}[\bar{1}01] \tag{12}$$

In the SISF mode, the [−1 0 1] dislocation dissociates into a pair of 1/3 [−2 1 1] and 1/3 [−1 −1 2] superpartial dislocations separated by an SISF, which can be expressed by

$$[\bar{1}01] \rightarrow \frac{1}{3}[\bar{2}11] + \mathrm{SISF} + \frac{1}{3}[\bar{1}\bar{1}2] \tag{13}$$

The energy criterion for the formation of APB dislocations proposed by Paidar et al. [51] can be given with the following inequality

$$\ln\left(\frac{8\pi\gamma_{\mathrm{SISF}}^{111}}{a_0 C_{44}}\right) \geq 2\ln\left(\frac{4\pi\gamma_{\mathrm{APB}}^{111}}{a_0 C_{44}}\right) + 1 \tag{14}$$

where $\gamma^{111}{}_{\mathrm{SISF}}$ and $\gamma^{111}{}_{\mathrm{APB}}$ are the SISF and APB energies on the (1 1 1) plane, respectively. Apparently, the competition between the two modes is closely related to the difference between the SISF and APB energies.

The SISF energy (γ_{SISF}) and APB energy (γ_{APB}) of the $L1_2$-$Co_3(Ti,M)$ structures in the fault region were calculated, and the results are summarized in Table 3. The values of stoichiometric $L1_2$-Co_3Ti and Ni_3Al as well as the available data from previous studies are included for comparison. Our calculated planar fault energies of stoichiometric $L1_2$-Co_3Ti and Ni_3Al agree well with the those in previous studies [11,43,49], confirming that our calculations are reliable. The alloying elements induce a significant change in both the γ_{SISF} and γ_{APB} on the (1 1 1) plane. Particularly, the SISF energy varies from 145 mJ/m^2 for $L1_2$-Co_3Ti to 89 mJ/m^2 for $L1_2$-Co_3(Ti,Mo), with a ~39% decrease. The APB energy of $L1_2$-Co_3(Ti,Ta) increases by ~15%, whereas that of $L1_2$-Co_3(Ti,Y) decreases by ~10%, as compared with that of $L1_2$-Co_3Ti.

Since the deformation behavior is sensitive to the γ_{SISF} and γ_{APB} on the (1 1 1) plane, the alloying effects on the $\gamma_{\mathrm{SISF}}/\gamma_{\mathrm{APB}}$ ratio of the $L1_2$-Co_3(Ti,M) compounds are illustrated in Fig. 10a. Y, Zr, Hf, V, Nb, Ta, Cr, Mo, and W significantly decrease the $\gamma_{\mathrm{SISF}}/\gamma_{\mathrm{APB}}$ ratio of the $L1_2$-Co_3(Ti,M) compounds, which may inhibit the formation of APBs. In addition, it is interesting to note that the $\gamma_{\mathrm{SISF}}/\gamma_{\mathrm{APB}}$ ratio of $L1_2$-Co_3(Ti,M) decreases with increasing atomic number of alloying elements in each period; that is, Cr, Mo, and W have a significant influence on the decrease in the $\gamma_{\mathrm{SISF}}/\gamma_{\mathrm{APB}}$ ratio. Fig. 10b plots

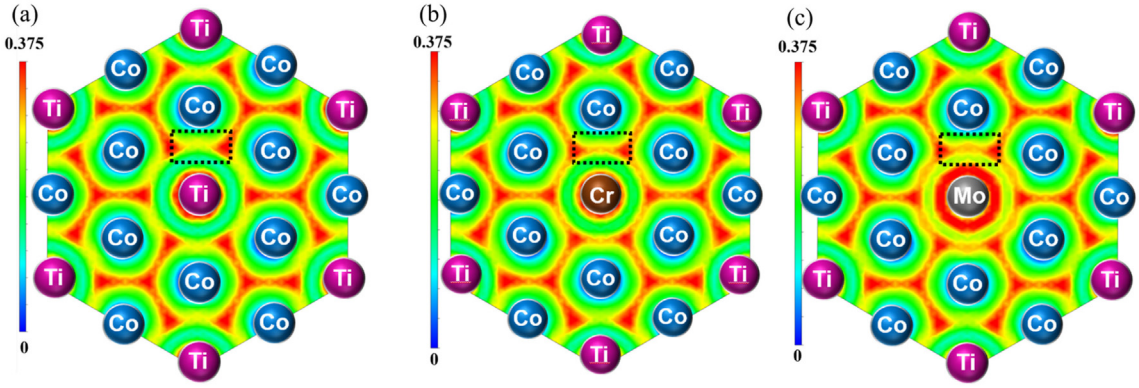

Fig. 9 – Contour plots of electron localization function (ELF) on the (1 1 1) plane of (a) $Co_{24}Ti_8$, (b) $Co_{24}(Ti_7Cr)$, and (c) $Co_{24}(Ti_7Mo)$.

Table 3 – Planar fault energies, including the superlattice SISF energy (γ_{SISF}) and APB energy (γ_{APB}), of the $Co_3(Ti,M)$ structures with 6.25 at.% M in the fault region. The superscript indicates the slip plane. The data of lattice constants (a_0), elastic constants (C_{44}), and Zener anisotropy (A_Z) of the $Co_3(Ti,M)$ structures were obtained from 32-atom supercells with an alloying concentration of 6.25 at.%.

System	$\gamma^{111}{}_{SISF}$ (mJ/m^2)	$\gamma^{111}{}_{APB}$ (mJ/m^2)	$\gamma^{010}{}_{APB}$ (mJ/m^2)	a_0 (Å)	C_{44} (GPa)	A_Z
Ni_3Al	65	190	100	3.569	128	2.89
Ref. [49]	59	190	107	3.571	128	2.92
Ref. [11]	70	192	95	–	–	–
Ref. [43]	72	205	–	3.57	125	2.78
Ref. [32]	–	–	–	3.56	129	2.90
Co_3Ti	145	306	315	3.606	121	2.37
Ref. [11]	147	312	308	–	–	–
Ref. [49]	149	308	308	–	143	2.79
Ref. [32]	–	–	–	3.61	119	2.48
Co_3(Ti, Sc)	136	282	308	3.635	106	2.42
Co_3(Ti, Y)	122	276	297	3.676	91	2.36
Co_3(Ti, Zr)	128	324	312	3.644	112	2.21
Co_3(Ti, Hf)	138	337	320	3.636	115	2.22
Co_3(Ti, V)	131	304	307	3.588	131	2.23
Co_3(Ti, Nb)	120	340	313	3.616	127	2.26
Co_3(Ti, Ta)	132	353	321	3.617	127	2.26
Co_3(Ti, Cr)	99	293	292	3.580	137	2.34
Co_3(Ti, Mo)	89	321	295	3.601	137	2.45
Co_3(Ti, W)	106	343	308	3.601	140	2.46

the boundary map for the APB and SISF dissociation schemes of a parent [−1 0 1] dislocation in $L1_2$ compounds. The results show that the $L1_2$-$Co_3(Ti,M)$ compounds with 6.25 at.% solute elements in the fault region satisfy the energy criterion for the formation of APB dislocations. Although the $L1_2$-$Co_3(Ti,M)$ compounds with additions of Cr, Mo, and W are in the region of the APB dislocation mode, they are close to the boundary between the APB and SISF dissociation regions. High contents of additions of Cr, Mo and W may change the deformation mode of the $L1_2$-$Co_3(Ti, M)$ compounds from APB-favored to SISF-favored ones.

3.3.2. *Yield strength anomaly*

One of the important characteristics of plastic deformation for the retention of high-temperature strength in superalloys is the yield strength anomaly [49]. It is generally documented that the yield strength anomaly is caused by the thermally activated cross-slip of screw dislocations gliding from the (1 1 1) to the (0 1 0) plane, leading to the formation of Kear-Wilsdorf (K–W) locks. The yield strength anomaly at high temperatures require two necessary criteria [52]: (1) the APB deformation mode is thermodynamically more stable than the SISF deformation mode, and (2) the dislocation dissociation on the (0 1 0) plane is more energetically favorable than that on the (1 1 1) plane. For the former requirement, the alloying effects on the APB and SISF deformation modes are discussed in Section 3.3.1. For the latter criteria, Saada et al. [53,54] proposed an energy-based condition, which can be described by

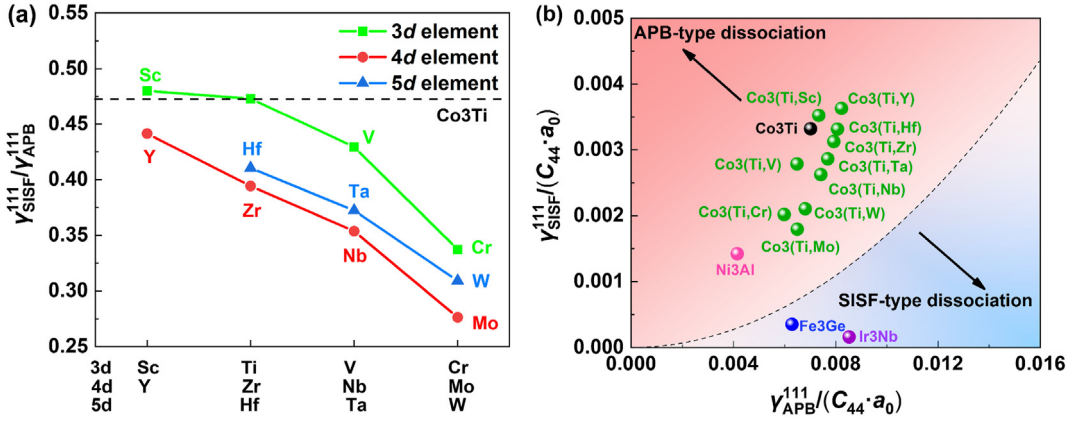

Fig. 10 – (a) $\gamma_{SISF}/\gamma_{APB}$ ratio on the (1 1 1) plane of $L1_2$-$Co_3(Ti,M)$ (M = Cr, Mo, W, V, Nb, Ta, Zr, Hf, Sc, and Y), and (b) boundary map for the APB- and SISF-type dissociation schemes of a parent [−1 0 1] dislocation in $L1_2$ compounds. The critical line refers to the Paidar's criteria [51]. The data of $L1_2$ Co_3Ti, Ni_3Al, and $Co_3(Ti,M)$ are from Table 3, while that of $L1_2$ Fe_3Ge and Ir_3Nb are from Refs. [49,50], respectively.

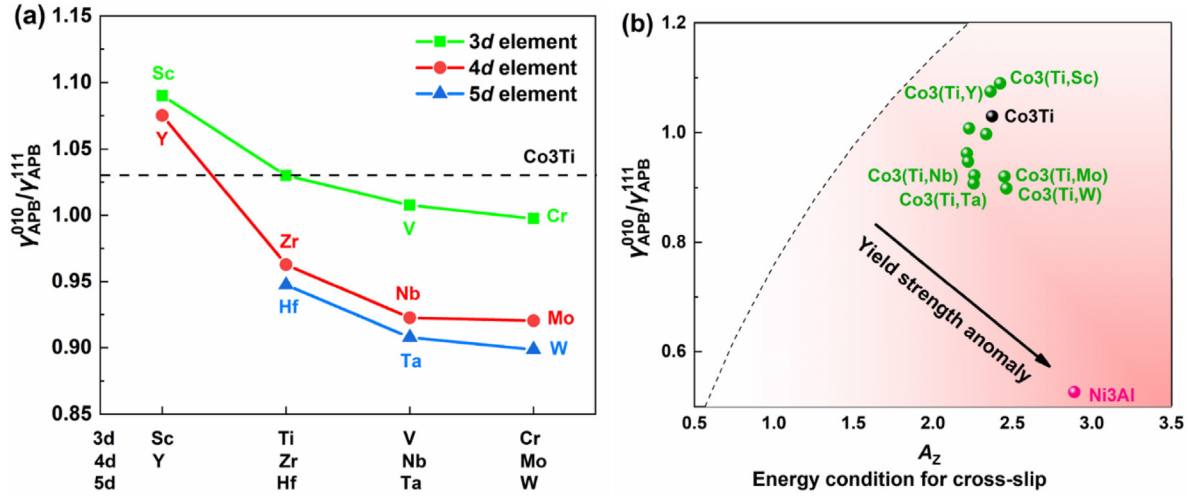

Fig. 11 – (a) λ of $L1_2$-Co_3(Ti,M) (M = Cr, Mo, W, V, Nb, Ta, Zr, Hf, Sc, and Y), and (b) λ–A_Z plot for the $L1_2$ Ni_3Al and Co_3(Ti,M). The dashed line refers to Saada's criteria [53].

$$\lambda < 3^{1/4} D_{ani}^{1/2} \tag{15}$$

$$\lambda = \gamma_{APB}^{010} / \gamma_{APB}^{111} \tag{16}$$

$$D_{ani} = 3^{1/2} A_Z / (A_Z + 2) \tag{17}$$

where λ is the APB anisotropy ratio, which is the ratio of the APB energy in the (0 1 0) plane (γ^{010}_{APB}) to that in the (111) plane (γ^{111}_{APB}), D_{ani} is a material parameter depending on the Zener anisotropy, and A_Z is the Zener anisotropy ($A_Z = 2C_{44}/(C_{11}-C_{12})$). If the inequality of Eq. (15) is satisfied, the dissociated screw superdislocation on the (0 1 0) plane is more energetically favorable than that on the (1 1 1) plane, which would facilitate the occurrence of yield strength anomaly, even if the initial cross-slip driving force may be negative. If the inequality is not satisfied, the dissociated screw superdislocation on the (0 1 0) plane is less stable than that on the (1 1 1) plane and the occurrence of yield strength anomaly would be inhibited [53,54]. From Eqs. (15)–(17), it can be seen that λ and A_Z are two key factors determining the occurrence of the yield strength anomaly.

To demonstrate the alloying effects on the yield strength anomaly, the APB energy on the (0 1 0) and (1 1 1) planes and the Zener anisotropy of the $L1_2$-Co_3(Ti,M) structures with an alloying concentration of 6.25 at.% were calculated, and the results are listed in Table 3. It is found the A_Z values of $L1_2$-Co_3(Ti,M) vary in the range of 2.21–2.46, which are comparable to that of $L1_2$-Co_3Ti (2.37). In other words, the alloying elements, including Cr, Mo, W, V, Nb, Ta, Zr, Hf, Sc, and Y, do not have a significant impact on the Zener anisotropy. Fig. 11a plots the alloying effects on the APB anisotropy ratio ($\gamma^{010}_{APB}/\gamma^{111}_{APB}$). It is apparent that the APB anisotropy ratio of $L1_2$-Co_3(Ti,M) decreases with increasing atomic number of alloying elements in each period, especially for those in the 4*d* and 5*d* groups. In particular, Nb, Ta, Mo, and W substantially decrease the APB anisotropy ratio of the $L1_2$-Co_3(Ti,M) compounds. Based on the data from Table 3, the alloying effects on the yield strength anomaly is shown in Fig. 11b. All the $L1_2$-Co_3(Ti,M) compounds satisfy the energy-based condition for the occurrence of yield strength anomaly. With the Nb, Ta, Mo, and W additions, the tendency of yield strength anomaly becomes more significant, as compared with that of $L1_2$-Co_3Ti. Therefore, our calculations suggest that the yield strength anomaly of the $L1_2$-Co_3(Ti,M) compounds is controlled mainly by the APB anisotropy ratio, other than the Zener anisotropy. It should be pointed out that this study focuses on the K–W mechanism for the occurrence of YSA, while other mechanisms, such as the activation of multiple slip modes within $L1_2$ phases [55] and the shearing of $L1_2$ phases via the SISF formation at high temperatures [56], may also contribute to the occurrence of the yield strength anomaly, which, however, is out of the scope of the present work and will be studied in future work.

4. Conclusions

The alloying effects on the site preference, structural stability, mechanical properties, and deformation behavior of $L1_2$-Co_3(Ti,M) were systematically studied by using first-principles calculations based on the density functional theory. The site preference of alloying elements was determined by comparing the transfer energy of alloying elements switching from the Co to Ti site. The structural stability was predicted by evaluating the formation enthalpy and energy difference between the $L1_2$ and $D0_{19}$ structures. The alloying effects on the mechanical properties, including elastic moduli and ideal shear strength, were critically studied. Finally, the effects of alloying additions on the deformation behavior and the tendency for the occurrence of yield strength anomaly were discussed in terms of the SISF energy, anisotropy of the APB energy, and elastic anisotropy. The conclusions can be drawn as follows.

1. Cr, Mo, W, V, Nb, Ta, Zr, Hf, Sc, and Y prefer to occupy the Ti site in $L1_2$-Co_3Ti. Among these alloying elements, Sc and Y exhibit a weak Ti-site preference, while all others show a strong Ti-site preference.
2. Cr, Mo, W, V, Nb, Ta, Zr, Hf, Sc, and Y reduce the structural stability of $L1_2$-Co_3(Ti,M). Thus, the solute concentration is important for the control of thermodynamic stability of the $L1_2$ structures.
3. The elastic moduli and ideal shear strength of $L1_2$-Co_3(Ti,M) increases with increasing average electron density. The strengthening effect of the alloying additions is due mainly to the strong covalent bonding between Co and alloying elements.
4. The competition between the APB and SISF deformation modes is closely related to the $\gamma_{SISF}/\gamma_{APB}$ ratio. The $\gamma_{SISF}/\gamma_{APB}$ ratio of $L1_2$-Co_3(Ti, M) decreases with increasing atomic number of alloying elements in each period in the range of studied elements, contributing to the change of deformation mode from the APB-favored to SISF-favored ones.
5. Alloying with Cr, Mo, W, V, Nb, Ta, Zr, and Hf decreases the APB anisotropy ratio of the $L1_2$-Co_3(Ti,M) compounds, while the Zener anisotropy shows no significant changes. The APB anisotropy ratio of the $L1_2$-Co_3(Ti,M) compounds decreases with increasing atomic number of alloying elements in each period, contributing to the yield strength anomaly.

Declaration of competing interest

The authors declare that they have no known competing financial interests or personal relationships that could have appeared to influence the work reported in this paper.

Acknowledgements

This research was supported by the National Natural Science Foundation of China (52171162), Research Grants Council of Hong Kong (ECS 25202719, GRF 15227121, C1017-21 GF, and C1020-21 GF), State Key Laboratory of Long-Life High Temperature Materials Open Fund (P0036623), Shenzhen Science and Technology Program (JCYJ20210324142203009), Research Institute for Advanced Manufacturing at PolyU (P0041364), and Guangzhou Science & Technology and Innovation Commission (P0030324).

Appendix A. Supplementary data

Supplementary data to this article can be found online at https://doi.org/10.1016/j.jmrt.2023.03.099.

REFERENCES

[1] Pauzi AA, Ghazali MJ, Zamri WFW, Rajabi A. Wear characteristics of superalloy and hardface coatings in gas turbine applications–a review. Metals 2020.
[2] Zhao JC, Westbrook JH. Ultrahigh-temperature materials for jet engines. MRS Bull 2003;28(9):622–30.
[3] Ruan JJ, Liu XJ, Yang SY, Xu WW, Omori T, Yang T, Deng B, Jiang HX, Wang CP, Kainuma R, Ishida K. Novel Co-Ti-V-base superalloys reinforced by L12-ordered γ′ phase. Intermetallics 2018;92:126–32.
[4] Sato J, Omori T, Oikawa K, Ohnuma I, Kainuma R, Ishida K. Cobalt-Base high-temperature alloys. Science 2006;312(5770):90–1.
[5] Bauer A, Neumeier S, Pyczak F, Göken M. Creep strength and microstructure of polycrystalline γ′-strengthened cobalt-base superalloys. Superalloys 2012;12:695–703.
[6] Pollock TM, Dibbern J, Tsunekane M, Zhu J, Suzuki A. New Co-based γ-γ′ high-temperature alloys. JOM 2010;62(1):58–63.
[7] Tsukamoto Y, Kobayashi S, Takasugi T. The stability of γ′-Co3(Al,W) phase in Co-Al-W ternary system. Mater Sci Forum 2010;654–656:448–51.
[8] Yan HY, Vorontsov VA, Dye D. Alloying effects in polycrystalline γ′ strengthened Co–Al–W base alloys. Intermetallics 2014;48:44–53.
[9] Jiang M, Saren G, Yang S-y, Li H-x, Hao S-m. Phase equilibria in Co-rich region of Co-Ti-Ta system. Trans Nonferr Metal Soc 2011;21(11):2391–5.
[10] Takasugi T, Hirakawa S, Izumi O, Ono S, Watanabe S. Plastic flow of Co3 Ti single crystals. Acta Metall 1987;35(8):2015–26.
[11] Im HJ, Lee S, Choi WS, Makineni SK, Raabe D, Ko W-S, Choi P-P. Effects of Mo on the mechanical behavior of γ/γ'-strengthened Co-Ti-based alloys. Acta Mater 2020;197:69–80.
[12] Im HJ, Makineni SK, Gault B, Stein F, Raabe D, Choi P-P. Elemental partitioning and site-occupancy in γ/γ′ forming Co-Ti-Mo and Co-Ti-Cr alloys. Scripta Mater 2018;154:159–62.
[13] Zenk CH, Povstugar I, Li R, Rinaldi F, Neumeier S, Raabe D, Göken M. A novel type of Co–Ti–Cr-base γ/γ′ superalloys with low mass density. Acta Mater 2017;135:244–51.
[14] Perdew JP, Wang Y. Accurate and simple analytic representation of the electron-gas correlation energy. Phys Rev B 1992;45(23):13244–9.
[15] Perdew JP, Burke K, Wang Y. Generalized gradient approximation for the exchange-correlation hole of a many-electron system. Phys Rev B 1996;54(23):16533–9.
[16] Ruban AV, Skriver HL. Calculated site substitution in ternary γ'-Ni3Al: temperature and composition effects. Phys Rev B 1997;55(2):856–74.
[17] Jiang C, Gleeson B. Site preference of transition metal elements in Ni3Al. Scripta Mater 2006;55(5):433–6.
[18] Wang C, Zhang C, Wang Y, Han J, Xu W, Liu X. Effects of transition elements on the structural, elastic properties and relative phase stability of L12 γ′-Co3Nb from first-principles calculations. Metals 2021;11(6).
[19] Xu WW, Shang SL, Wang CP, Gang TQ, Huang YF, Chen LJ, Liu XJ, Liu ZK. Accelerating exploitation of Co-Al-based superalloys from theoretical study. Mater Des 2018;142:139–48.
[20] Sun J, Du W, Xiao B, Wu Y, Liu Y, Zhang T. First-principles study of multiple-site substitutions of alloying elements in Ni-based single crystal superalloys. Sci China Technol Sci 2021;64(6):1276–84.
[21] Tang Y, Xiao B, Chen J, Liu F, Du W, Guo J, Liu Y, Liu Y. Multi-component alloying effects on the stability and mechanical properties of Nb and Nb–Si alloys: a first-principles study. Metall Mater Trans 2023;54(2):450–72.
[22] Guo J, Xiao B, Li Y, Zhai D, Tang Y, Du W, Liu Y. Machine learning aided first-principles studies of structure stability of Co3(Al, X) doped with transition metal elements. Comput Mater Sci 2021;200:110787.
[23] Kittel C, McEuen P. Introduction to solid state physics. John Wiley & Sons; 2018.

[24] Shang S, Wang Y, Liu Z-K. First-principles elastic constants of α- and θ-Al2O3. Appl Phys Lett 2007;90(10):101909.
[25] Sun Z, Li S, Ahuja R, Schneider JM. Calculated elastic properties of M2AlC (M=Ti, V, Cr, Nb and Ta). Solid State Commun 2004;129(9):589–92.
[26] Kim DE, Shang SL, Liu ZK. Effects of alloying elements on elastic properties of Ni3Al by first-principles calculations. Intermetallics 2010;18(6):1163–71.
[27] Chen Y, He S, Yi Z, Peng P. Impact of correlative defects induced by double Re-addition on the ideal shear strength of γ′-Ni3Al phases. Comput Mater Sci 2018;152:408–16.
[28] Rao L, Liu H, Shao W, Liu H, Xing X, Zhou Y, Shi Z, Yang Q. Tailoring the mechanical properties of diamond-like carbon film by doping of trace nonmetal elements: a first-principles study. J Alloys Compd 2021;868:159151.
[29] Roundy D, Krenn CR, Cohen ML, Morris JW. Ideal shear strengths of fcc aluminum and copper. Phys Rev Lett 1999;82(13):2713–6.
[30] Qiu S, Zhang X-C, Zhou J, Cao S, Yu H, Hu Q-M, Sun Z. Influence of lattice distortion on stacking fault energies of CoCrFeNi and Al-CoCrFeNi high entropy alloys. J Alloys Compd 2020;846:156321.
[31] Zenk CH, Neumeier S, Stone HJ, Göken M. Mechanical properties and lattice misfit of γ/γ′ strengthened Co-base superalloys in the Co–W–Al–Ti quaternary system. Intermetallics 2014;55:28–39.
[32] Jain A, Ong SP, Hautier G, Chen W, Richards WD, Dacek S, Cholia S, Gunter D, Skinner D, Ceder G, Persson KA. Commentary: the Materials Project: a materials genome approach to accelerating materials innovation. Apl Mater 2013;1(1):011002.
[33] Cruz-Gandarilla F, Gayosso-Armenta R, Hesiquio-Garduño M, Cabañas-Moreno JG, Martínez-Sánchez R. XRD studies of Co-Fe-Ti nanocrystalline intermetallics. Mater Sci Forum 2003;442:109–14.
[34] Verma SK, Pramanik A, Jyothsna K, Vamsi KV, Karthikeyan S. Phase transformation temperatures, γ–γ′ lattice parameter misfit, and γ′ precipitate morphology in Co–Ti–V alloys. Metall Mater Trans A 2022;53(11):4011–22.
[35] Yoo B, Im HJ, Seol J-B, Choi P-P. On the microstructural evolution and partitioning behavior of L12-structured γ′-based Co-Ti-W alloys upon Cr and Al alloying. Intermetallics 2019;104:97–102.
[36] Li L, Wang C, Chen Y, Yang S, Yang M, Zhang J, Lu Y, Han J, Liu X. Effect of Re on microstructure and mechanical properties of γ/γ' Co-Ti-based superalloys. Intermetallics 2019;115:106612.
[37] Chen K, Bielawski M. Interfacial fracture toughness of transition metal nitrides. Surf Coat Technol 2008;203(5):598–601.
[38] Chen X-Q, Niu H, Li D, Li Y. Modeling hardness of polycrystalline materials and bulk metallic glasses. Intermetallics 2011;19(9):1275–81.
[39] Xu WW, Han JJ, Wang ZW, Wang CP, Wen YH, Liua XJ, Zhu ZZ. Thermodynamic, structural and elastic properties of Co3X (X = Ti, Ta, W, V, Al) compounds from first-principles calculations. Intermetallics 2013;32:303–11.
[40] Senkov ON, Miracle DB. Generalization of intrinsic ductile-to-brittle criteria by Pugh and Pettifor for materials with a cubic crystal structure. Sci Rep 2021;11(1):4531.
[41] Liu X, Wang Y, Xu W-W, Han J, Wang C. Effects of transition elements on the site preference, elastic properties and phase stability of L12 γ′-Co3(Al, W) from first-principles calculations. J Alloys Compd 2020;820:153179.
[42] Rose JH, Shore HB. Uniform electron gas for transition metals: input parameters. Phys Rev B 1993;48(24):18254–6.
[43] Shang S-L, Shimanek J, Qin S, Wang Y, Beese AM, Liu Z-K. Unveiling dislocation characteristics in Ni3Al from stacking fault energy and ideal strength: a first-principles study via pure alias shear deformation. Phys Rev B 2020;101(2):024102.
[44] Ogata S, Li J, Yip S. Ideal pure shear strength of aluminum and copper. Science 2002;298(5594):807–11.
[45] Xia F, Xu W, Shi Z, Xie W, Chen L. Exploring the alloying effects on generalized stacking fault energy and ideal strength of Ni and Ni3Al phases in Ni-based superalloys. Mech Mater 2022;165:104183.
[46] Qiu S, Miao N, Zhou J, Guo Z, Sun Z. Strengthening mechanism of aluminum on elastic properties of NbVTiZr high-entropy alloys. Intermetallics 2018;92:7–14.
[47] Becke AD, Edgecombe KE. A simple measure of electron localization in atomic and molecular systems. J Chem Phys 1990;92(9):5397–403.
[48] Guo Z, Zhu L, Zhou J, Sun Z. Microscopic origin of MXenes derived from layered MAX phases. RSC Adv 2015;5(32):25403–8.
[49] Vamsi KV, Karthikeyan S. Deformation modes and yield strength anomaly in L12 compounds. J Alloys Compd 2021;860:158411.
[50] Okamoto NL, Takemoto S, Chen ZMT, Yamaguchi M, Inui H. FCC metal-like deformation behaviour of Ir3Nb with the L12 structure. Int J Plast 2017;97:145–58.
[51] Paidar V, Pope DP, Yamaguchi M. Structural stability and deformation behavior of L12 ordered alloys. Scripta Metall 1981;15(9):1029–31.
[52] Liu JB, Johnson DD, Smirnov AV. Predicting yield-stress anomalies in L12 alloys: Ni3Ge–Fe3Ge pseudo-binaries. Acta Mater 2005;53(13):3601–12.
[53] Saada G, Veyssiere P. The dissociation of a screw superdislocation in the L12 structure. Philos Mag A 1992;66(6):1081–103.
[54] Paxton AT, Sun YQ. The role of planar fault energy in the yield anomaly in L12 intermetallics. Philos Mag A 1998;78(1):85–104.
[55] Suzuki A, DeNolf GC, Pollock TM. Flow stress anomalies in γ/γ′ two-phase Co–Al–W-base alloys. Scripta Mater 2007;56(5):385–8.
[56] Bezold A, Volz N, Lenz M, Zenk CH, Spiecker E, Mills M, Göken M, Neumeier S. Yielding behavior of a single-crystalline γ'-strengthened Co-Ti-Cr superalloy. Scripta Mater 2021;200:113928.